Journal of Applied Fluid Mechanics, Vol. 16, No. 7, pp. 1467-1482, 2023.
Available online at www.jafmonline.net, ISSN 1735-3572, EISSN 1735-3645.
https://doi.org/10.47176/jafm.16.07.1748

Aerodynamic Drag Improvements on a Simplified Heavy Vehicle using Three-sided Plain and Notched Base Flaps

E. Fırat†

Department of Mechanical Engineering, Faculty of Engineering, Munzur University, Tunceli, 62000, Turkey

†*Corresponding Author Email: efirat@munzur.edu.tr*

(Received January 4, 2023; accepted March 12, 2023)

ABSTRACT

An experimental investigation has been undertaken to determine the effects of plain and notched base flaps on the drag performance of simplified tractor-trailer combination without any intermediate gap, Generalized European Transport System (GETS). Both plain and notched base flaps are rigid, made up of three identical flaps whose length is equal to the width of the GETS model, and not angled inward or outward. The experiments examined three-sided flap configurations corresponding to various combinations of seven heights of the plain part (from 10 to 40 mm in steps of 5 mm), four notch amplitudes (from 2.5 to 10 mm in steps of 2.5 mm), and five notch wavelengths (from 10 to 50 mm in steps of 10 mm). It is shown that the drag performance of the plain flap at zero yaw highly depends on the height of the plain flap. The maximum drag reduction occurs for e/w=0.1 yielding a drag reduction of 1.9% when compared to the GETS model without flap (baseline GETS). It was shown that the time-averaged drag coefficient increased slightly until a maximum was reached at e/w=0.3 but then decreased slightly with increasing e/w. Under zero yaw angle conditions, GETS model with a notched base flap, e10-a05.0-λ20, gives the lowest drag. The addition of this base flap to the GETS model resulted in a 2.8% drag reduction. This notched base flap was shown to be more effective not only at reducing $<C_D>$ under yawed flow conditions tested but also at reducing time-averaged side coefficient under yawed flow conditions tested, compared to the e10-a00.0-λ00 flap.

Keywords: Passive flow control; Drag reduction; Plain base flap; Notched base flap; Simplified heavy vehicle; Cross-wind.

NOMENCLATURE

A_F	frontal area of the GETS model	P	static pressure
a	notch amplitude	Re_w	width-based Reynolds number
a/w	dimensionless notch amplitude	Tu_x	freestream turbulence intensity
C_D	drag coefficient	U_∞	freestream velocity
C_{Mz}	moment coefficient	w	width of the model
C_P	pressure coefficient	x	streamwise coordinate direction
$C_{P\text{-}RMS}$	root-mean-square pressure coefficient	y	transverse coordinate direction
C_S	side coefficient	z	spanwise coordinate direction
e	height of the plain part of a flap		
e/w	dimensionless height of the plain part of a flap	$<..>$	time-averaging operator
F_D	drag force	β	yaw angle
F_S	side force	Δ	difference
g	ground clearance	λ	notch wavelength
h	height of the model	λ/w	dimensionless notch wavelength
l	length of the model	μ	viscosity of the air
M_z	pitching moment	ρ	density of the air

1. INTRODUCTION

It is reported that CO2 emissions from heavy-duty vehicles (i.e., trucks and buses) represented about 25% of total road transport CO2 emissions in the European Union in 2016 (Regulation (EU) 2019/1242, 2019). It is also reported that large trucks (10 tons or more) were responsible for 65%

to 70% of all CO2 emissions from heavy-duty vehicles (HDVs). This explains why the first-ever CO2 emission standards, adopted in 2019, initially covered only new large trucks.

As a large truck, the current European tractor-trailer combination resembles a long rectangular prism that has a rounded front and a flat back face. This unstreamlined shape, of course, plays an essential role in maximizing load volume in the permissible dimensions of a vehicle (Directive 96/53/EC, 1996; Directive (EU) 2015/719, 2015). However, the mentioned shape has poor aerodynamic performance due largely to high pressure (form) drag. This explains why approximately 40% of the total energy required to move a 40-tons European heavy truck at a highway speed of 85 km/h has to be used to overcome air resistance (Verband der Automobilindustrie e.V. 2010). This ratio is, of course, reduced at present due to aerodynamic improvements to HDVs.

Reducing HDV fuel consumption is a significant challenge for both environmental and economic reasons. Truck platooning is one way of simultaneously improving fuel efficiency and reducing CO2 emissions without compromising overall load space (Veldhuizen *et al.* 2019; Törnell *et al.* 2021). This is also valid for light-duty vehicles (LDV; Cerutti *et al.* 2021). Another way is to attach various passive (PFCD) and/or active flow control devices (AFCD) to some parts of the HDV surfaces. These devices can be used either individually or as a group to increase aerodynamic efficiency of HDV (Landman *et al.* 2010; McAuliffe 2015; Salati *et al.* 2017; Schmidt *et al.* 2018; Hariram *et al.* 2019; Seyhan and Sarioglu 2021), even aerodynamic efficiency of LDV (Urquhart *et al.* 2020; Haffner *et al.* 2022). Some of them were developed by tractor manufacturers and are now standard on all new HDVs. Some of them are already available on the market such as roof air deflector/roof fairing, cab side extender, and trailer skirt. Some of them are under development or are being designed for development.

Aerodynamic losses are non-recoverable. For the highway environment, they are the dominant source for power and fuel consumption (Patten *et al.* 2012). Front, top, and sides of the cab, the gap between the tractor and the trailer, the underbody of the tractor-trailer combination, and the rear surface of the trailer are the key energy loss areas on a typical tractor-trailer combination. Any flow control device which is attached to the front surface of the tractor must not limit the driver's field of direct and indirect vision. This narrows the number of devices to a few (e.g. active grill shutters, cab side-edge turning vanes; Hariram *et al.* 2019). PFCDs such as cab roof deflector, cab roof fairing with or without a collar, aerodynamic mirrors, and tractor chassis filler panels are producing significant reductions in drag acting on the top and sides of the cab as well as the gap between the tractor and the trailer, especially when used in a combined manner after a careful optimization and evaluation (McAuliffe 2015; Salati *et al.* 2017; McArthur *et al.* 2018; Kim *et al.* 2019; Hariram *et al.* 2019). Air dam, trailer side panels (trailer side skirts), cab side panels, bogie fairings, aerodynamic wheel covers, and slotted mudflaps are examples of PFCDs used to reduce the drag associated with the tractor-underbody and trailer-underbody (McAuliffe 2015; McArthur *et al.* 2018; Hariram *et al.* 2019; Kim *et al.* 2019). For the trailer aerodynamic technologies, base flap, base cavity, and boat-tail are effective PFCDs for reducing the drag contribution from the large region of separated flow at the rear of a trailer (McAuliffe 2015; Schmidt *et al.* 2015; Hassaan *et al.* 2018; Kim *et al.* 2019; Rejniak and Gatto 2019; Hassaan *et al.* 2020).

Base flap looks promising for HDV industry (McAuliffe 2015). Compared to other passive flow control parts, it has very simple and thin parts, requires a low set-up cost, is quite light, is foldable, and is easy to install. Base flap have also proven to be effective at reducing the drag on simplified LDVs (passenger cars and vans; Beaudoin and Aider 2008; Kowata *et al.* 2008; Hanfeng *et al.* 2016; Kim *et al.* 2016; Garcia de la Cruz *et al.* 2017; Capone and Romano 2019). In previous experimental studies on base flap drag reduction, the effectiveness of some parameters was demonstrated. The first of them is flap angle which formed by the intersection of the flap and the drag-axis at zero yaw. Browand *et al.* (2005) presented field test results for fuel savings by means of flaps that attached to the sides and top of the rear of the trailer (three-sided flaps). The flaps are approximately 61 cm (i.e. one-fourth of the trailer-base width) in length. The key parameter investigated in their study is the flap angle (i.e., 10°, 13°, 16°, 19°, and 22°). It is stated that the optimum flap angle appears to be 13°, for which the fuel consumption is 0.3778±0.0025 L/km compared to the no flaps case of 0.3941± 0.0034 L/km. The second of them is flap shape (i.e., planar or curved, tapered or not). Smith *et al.* (2007) assessed the effectiveness of curved and straight three-sided (top and sides) base plates in reducing drag. It was shown that the curved plate provided slightly more drag reduction at a flap angle of 5°, but slightly less drag reduction at a flap angle of 12.5°. McAuliffe (2015) tested drag reduction performance of a three-sided base flap (top and sides) with 1:4 tapered side flaps and a non-tapered top flap. It is stated that this base flap provides a drag reduction of about -0.033 (-5.7%). However, this base flap was not compared to the non-tapered equivalent. Therefore, the influence of side-flap tapering on the performance of tractor-trailer model cannot be determined. The third one is the number of flaps. Kowata *et al.* (2008) investigated drag reduction on a 1:6 scale square-back bluff body (representative of a light-duty vehicle) by employing a rear underbody slant and base flap. Flaps at the top and sides were extended 20 mm into the wake and rounded with a radius of 50 mm (i.e. r/w=50/65). It was found that the aerodynamic performance of the square-back model with three-sided base flap (top and sides) demonstrates best performance in comparison to the same model with one-sided base flap (only top) for all underbody diffuser angles tested. The fourth one is the flap length. Capone and Romano (2019)

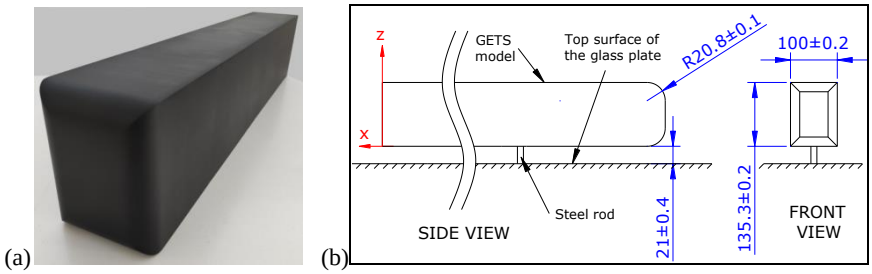

Fig. 1. (a) A close-up view of the baseline GETS model tested. (b) Schematic of the baseline GETS model showing the major dimensions (not to scale). All dimensions are in millimeters.

investigated the effects of angle of top flap, angle of side flaps, and the length of the side flaps on the near-wake structure and aerodynamic characteristics of a square-back model (representative of a light-duty vehicle) with non-rotating wheels. Three different side flaps, all with a height of 15 mm and a thickness of 1 mm, were tested. Each of the side flaps had a different length (i.e., small, 50 mm, mid-length, 100 mm, and full-length, 150 mm). It is shown that the flap length has a noticeable effect on the drag and lift performance. The model with mid-length side flaps not only demonstrates favorable downforce (negative lift) characteristics (a 130% increase in the downforce), but also shows the best drag performance (a 5% decrease in the drag) when compared to the baseline model. The fifth one is the flap height, that is, the distance from the bottom surfaces of flaps that are attached to the base surface to the top surfaces of flaps. This parameter must meet with local legislative requirements. For example, in the European Union (EU), any aerodynamic device and equipment exceeding 500 mm in height are to be type approved before being placed on the market (Directive (EU) 2015/719, 2015). Mason and Beebe (1978) made some modifications to the front and rear parts of a 1:7 scale tractor-trailer model in order to explore the practical potential for drag reduction. They also tested the effect of three-sided base flap and stated that a flap height of 0.13d (d=$(4A/\pi)^{0.5}$ where A is the frontal area of the model) reduced the drag coefficient by 0.03. However, the effects of flap height have yet to be demonstrated in any study of the base flap to date. This is the first motivation for the present investigation. The second motivation for the present investigation is that although there have been a great number of investigations concerned with the flaps behind a simplified or realistic HDV models, there are no papers whose focus has been to study the effect of base flap that breaks the separation line on the aerodynamic characteristics.

The first objective of the experimental investigation reported in this paper is to examine the effect of flap height of the three-sided plain base flap on the drag performance of the GETS model. The second objective is to examine the effects of the three-sided notched base flap on the drag performance of the GETS model. The key parameters investigated in this study were the dimensionless plain flap height (e/w), dimensionless notch amplitude (a/w), dimensionless notch wavelength (λ/w), and width-based Reynolds number (Re_w). Road vehicles usually experience terrestrial winds from all directions (Sumida and Hayakawa 2019; Levin and Chen 2022). In other words, they spend time being driven in conditions where the ambient wind is not usually stationary and not in-line with vehicle motion. Therefore, another key parameter investigated in this study was, yaw angle (β).

In addition, it will be seen later that Reynolds number independence in this wind tunnel tests has not been achieved. It is therefore not possible to obtain fairly accurate full-scale results. However, it was shown that a researcher does not need to match the Reynolds number of a small-scale square-back model in a wind tunnel with that of a full-scale prototype to assess the drag reducing potential of passive control parts attached to the base of a small-scale square-back model (Van Straaten 2007; Van Raemdonck 2012; Salati *et al.* 2017).

2. EXPERIMENTAL SETUP

2.1 Wind Tunnel

All experiments reported here were performed in the Karadeniz Technical University open circuit, low speed, and closed working section wind tunnel. The tunnel has a contraction ratio of about 6.3:1. A variable frequency drive was integrated with the electrical motor of the axial fan to achieve the desired freestream velocity (U_∞) in the test section. The tunnel has a 1200 mm long test section with inlet cross-section 570 mm wide by 570 mm high and outlet cross-section 583 mm wide by 583 mm high. The area-weighted freestream turbulence intensities (Tu_x) at freestream velocities of U_∞=8.0±0.2 m/s, 19±0.4 m/s, and 25±0.5 m/s, were 0.50%, 0.73%, and 1.0%, respectively. The width-based Reynolds numbers of the experimental study ranged from Re_w=51800±1200 (U_∞=8.0 m/s) to 162000±3800 (U_∞=25 m/s).

2.2 Experimental Model and Base Flap

The model used for this investigation was a 1:26 scale Generalized European Transport System (GETS) with a height (h) of 135.3±0.2 mm, a width (w) of 100.0 ±0.2 mm, and a length (l) of 635.8±0.3 mm (Fig. 1; Van Raemdonck and Van Tooren 2008). GETS model was dimensionally superior to the construction volume of the 3-D printing machine. Thus, it was split into three parts with straight cuts. The middle and rear parts of the GETS model have an empty space inside, but the front part

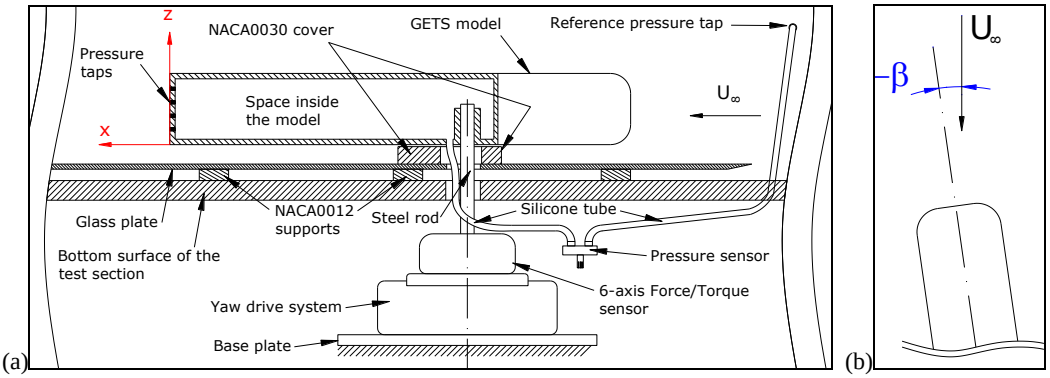

Fig. 2. (a) Schematic side view of the baseline GETS model at zero yaw in the wind tunnel. (b) Schematic top view of the GETS model with a yaw. Schematic drawings are not to scale.

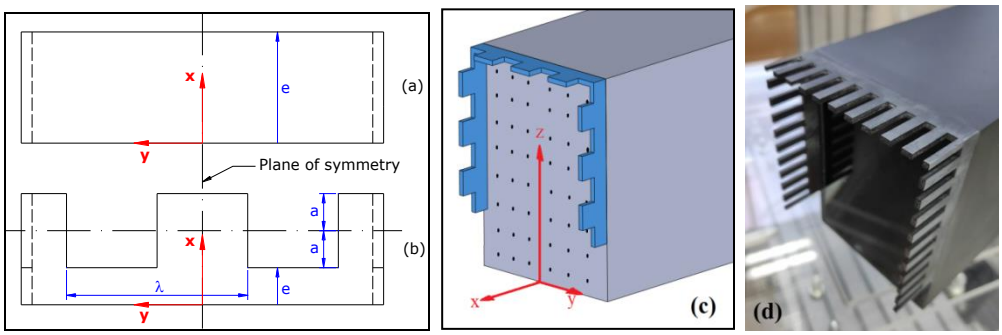

Fig. 3. Main types of three-sided base flap with geometric parameters: (a) Top view drawing of a plain base flap (i.e. e30-a00.0-λ00), (b) Top view drawing of a notched base flap (i.e. e10-a10.0-λ40), (c) The origin of the coordinate system and GETS model with a three-sided notched base flap, (d) Image of the base part of the GETS model with a notched flap. Thickness of the flaps printed is 3±0.1 mm.

of the GETS model (Fig. 2). The empty space is required to measure the static pressure on the rear surface of the GETS model (i.e. base). The wall thickness of the middle and rear parts is 2.4±0.1 mm. The walls of these parts may deflect inwards when subjected to wind loading. To prevent this, thin rectangular plate supports were added on the inside of the walls of these parts.

External surfaces of the parts were initially flattened by rubbing 120-grit, 180-grit, and 400-grit wet-and-dry sandpapers, respectively, over them after printing. The cyanoacrylate glue was then used to combine these parts. A mixture of polyester putty and hardener was used to smooth out unevenness in the above-mentioned external surfaces. And finally, these surfaces were made smooth by sanding them with 220-grit, 400-grit, and 600-grit sandpapers. The outside walls of the flaps were also sanded with 400-grit and 600-grit sandpapers, respectively. A very thin, double-sided adhesive tape was used to firmly attach base flap to GETS model and to fill the gap between base flaps and GETS model (i.e. sealing material). Prior to attachment, GETS model and all base flaps were painted black.

The GETS model was positioned in the center of the test section. At zero yaw, the maximum effective blockage for the working section above the glass ground plate was about 4.25%. No blockage correction was made since it was lower than 5% (SAE J1252, 1981). The model height was 0.28 of the active test section height. The ratio of the gap between the GETS model and the ground plate to model width (i.e., g/w) was 0.210±2%. The 4 mm thick ground plate was installed 12 mm above the inner surface of the bottom wall of the test section to reduce the thickness of the turbulent boundary layer. The thickness of the boundary layer developing on the ground plate at the GETS model front was 10.3±0.2 mm at Re_w=123000±2900. Ground plate extended 2.1w in front of the GETS model and 3.5w behind the GETS model. The maximum allowable yaw angle (β) in the test section that is measured by fixing the projection width of the GETS model to 0.3 of the tunnel width is β=6° (SAE J1252, 1981). Therefore, the yaw angles tested range from -6° to 6° in 1° increments. The uncertainties are 0.3° for both yaw and pitch angles.

The key flap parameters investigated in this study are shown in Fig. 3. The length of each flap is exactly equal to the width of the GETS model. The experiments examined three-sided base flap configurations corresponding to various combinations of seven es, from e=10 to 40 mm in steps of 5 mm, four as, from a=2.5 to 10 mm in steps of 2.5 mm, and five λs, from λ=10 to 50 mm in steps of 10 mm. Base flaps are coded based on these parameters as follows: They are firstly labeled by "e" followed by a number indicating the value of this parameter in mm. They are secondly labeled by "a" followed by a number indicating the value of this parameter in mm. And lastly, they are labeled "λ" followed by a number indicating the value of

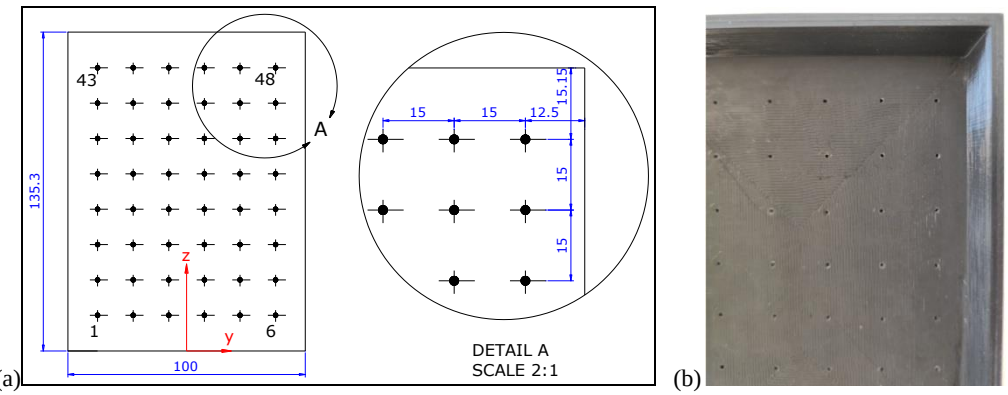

Fig. 4. (a) Rear view of the GETS model showing the locations and numbers of pressure taps. (b) A close-up view of the pressure taps in the base of the model with a plain base flap. All dimensions are in millimeters.

this parameter in mm. All parameters were separated by a hyphen (see the caption of Fig. 3 for examples). It must be noted that the height of the plain part is e=10 mm for all notched base flaps tested.

2.3 Force, Moment, and Pressure Measurements

GETS model connected by steel rod with a diameter of 12 mm to 6-axis force/torque (F/T) sensor (Schunk, FTD-Gamma SI-32-2.5) that was attached to a computer-controlled yaw drive system that allowed rotation of the GETS model around rods vertical axis (Fig. 2). The distance between the rod axis and the base was about 3.45w. No wheels or extra supports were used for the model. To avoid any corrections for tare forces and moments, parts of the silicone tube and steel rod between the GETS model and glass plate were enclosed by a hollow NACA0030 profile with a chord length of 66.6±0.2 mm. The height of this NACA profile is 19.0±0.2 mm. This profile was attached only onto the glass plate and not touching to GETS model, silicon tube, and steel rod even under non-zero yaw angle conditions. The relatively very small vortical structures shed from the NACA0030 profile presumably dissipated before they reached the base of the GETS model and do not have an effect on the flow characteristics in the GETS model wake. The F/T sensor was used to measure the time-averaged drag, $<F_D>$, time-averaged side, $<F_S>$, and time-averaged pitching moment, $<M_Z>$, experienced by the GETS model. Signals from the F/T sensor were sampled at 2 kHz for 30 s. The time-averaged drag coefficient, $<C_D>$, time-averaged side coefficient $<C_S>$, and time-averaged moment coefficient, $<C_{Mz}>$, are calculated as,

$$< C_D >= \frac{2 \cdot < F_D >}{\rho \cdot U_\infty^2 \cdot A_F} \quad (1)$$

$$< C_S >= \frac{2 \cdot < F_S >}{\rho \cdot U_\infty^2 \cdot A_F} \quad (2)$$

$$< C_{Mz} >= \frac{2 \cdot < M_z >}{\rho \cdot U_\infty^2 \cdot A_F \cdot l} \quad (3)$$

where ρ is the air density (kg/m^3) and A_F is the frontal area of the GETS model (m^2). For the sake of clarity, the operator "<...>" is used to indicate time-averaged quantities. The uncertainty in $<C_D>$ ranged from ±0.027 for Re_w=51800±1200 to ±0.014 for Re_w=162000±3800. The uncertainty in $<C_S>$ was estimated to be less than 0.02. The uncertainty in $<C_{Mz}>$ was estimated to be less than 0.003.

Pressure measurements were conducted at the rear surface of the GETS model (i.e., base) using 6 × 8 taps distributed along an equispaced grid with Δy=Δz=15±0.2 mm, as shown in Fig. 4. Measurements were made for the zero-yaw condition (β=0°). The figure also shows the exact locations and numbers of pressure taps with a diameter of 0.9±0.1 mm. Taps are perpendicular to the model base and distributed symmetrically referring to the vertical plane of symmetry of the model (i.e., x-z plane). A bundle of thin tubes were not preferred to connect the taps to a mechanical scanivalve system or pressure sensor. Instead, only one silicone tube with an inner diameter of 4.5 mm was used to connect the desired tap to the pressure sensor (Fig. 2). To measure the pressure in one tap, the remaining taps were closed by 4 mm × 4 mm, very thin sealing tapes. Briefly, the plugging method was preferred to the tubing method. The reference pressure is taken by a static tap mounted at the side surface of the test section (Fig. 2). To prevent air leaking into or out of the GETS model during force and pressure measurements, a sealant spray coating was also applied to the internal walls of the model. The static pressures were measured with a digital differential pressure sensor with a full-scale range of ±125 Pa (Sensirion, SDP810-125Pa). Pressure data were recorded at 250 Hz for 300 s. Base pressure measurements will be expressed in terms of the dimensionless pressure coefficient as

$$< C_P >= \frac{2 \cdot < \Delta P >}{\rho \cdot U_\infty^2} \quad (4)$$

where ΔP is the change in the surface pressure measured on the model base relative to the local static pressure measured at the reference pressure tap (Pa). The uncertainty in $<C_P>$ was estimated to be less than 4%.

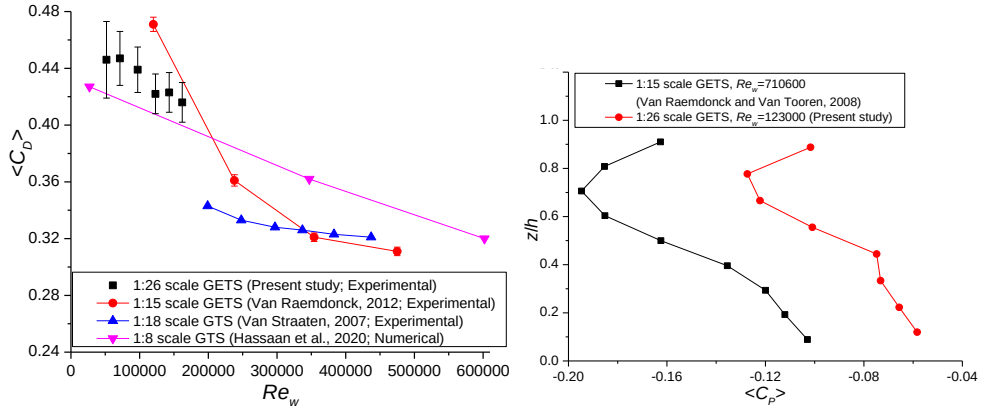

Fig. 5. Validation of experimental method. β=0°. The $\langle C_D \rangle$ for the GTS model is shown for comparison.

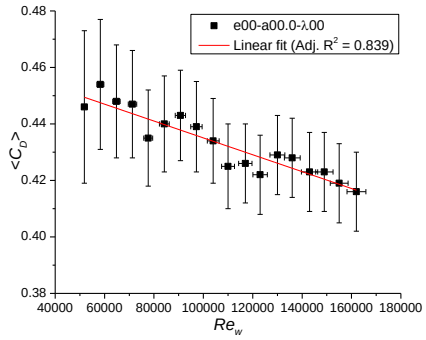

Fig. 6. Measurements of time-averaged drag coefficient versus width-based Reynolds number for a GETS model without base flap (i.e. e00-a00.0-λ00). β=0°. Uncertainties are drawn on graph as error bars.

2.4 Validation

Before assessing the effectiveness of various base flaps in terms of drag performance at relatively lower width-based Reynolds numbers, a series of measurements for comparison purposes were performed using baseline GETS and GTS models. This is required to analyze the validity of the experimental setup used in this study (Fig. 5). The assessment was made based on two criteria. The first one (left-hand plot) is the variation of the $\langle C_D \rangle$ relative to Re_w. The second one is variation of $\langle C_P \rangle$ along the height of the model base at y/w=0.

A $\langle C_D \rangle$ of 0.471±0.05 was reported by Van Raemdonck (2012) for the similar GETS configuration with stationary ground at $Re_w \approx 120000$. The difference of +0.049 (+11.2%) in $\langle C_D \rangle$ is caused mainly by one reason. His model has four roughness tapes with a thickness of 0.65 mm on the front surface. These tapes advance the transition from laminar to turbulent and prevent the flow separation from the front surface. It is also known that skin friction drag along a flat plate reaches its highest values when the flow becomes fully turbulent, and then exponentially decreases with increasing Reynolds number based on the distance from the leading edge of this plate (Çengel and Cimbala 2010). Compared to GETS model, GTS model is more aerodynamic in shape. This explains why GTS model shows better drag performance when compared to the GETS model. The $\langle C_P \rangle$ profiles in Fig. 5 show similar trends despite the distinctly different Re_w. Van Raemdonck (2012) showed that the baseline GETS model has a decreasing base $\langle C_P \rangle$ for an increasing Re_w. This explains why increasing the Re_w this much significantly decreased the $\langle C_P \rangle$ along the height of the model base by a relatively constant margin.

3. RESULTS AND DISCUSSION

3.1 Model without Base Flap (Baseline)

Figure 6 shows $\langle C_D \rangle$ measurements versus Re_w for the GETS model without a base flap (baseline). As Re_w increases the $\langle C_D \rangle$ gradually decreases from around 0.446 to 0.416. Hassaan *et al.* (2020) who numerically investigated the effect of geometric alterations on the near-wake structure of and $\langle C_D \rangle$ of the Ground Transportation System (GTS) found a similar trend at relatively low width-based Reynolds numbers ($2.7\times10^4 \leq Re_w \leq 0.6\times10^6$). This downward trend was also seen in the experimental study of Storms *et al.* (2001) between width-based Reynolds numbers of 300000 and 500000. They attributed this reduction to flow variations around the front of the GTS model.

Flow visualization results (not given here) on the top and sides of the GETS model revealed laminar separation bubbles immediately downstream of rounded edges. It it known that these bubbles act as a site of laminar to turbulent transition. It is also known that skin friction drag along a flat plate reaches its highest values when the flow becomes fully turbulent, and then exponentially decreases with increasing Reynolds number based on the distance from the leading edge of this plate (Çengel and Cimbala 2010). This is the main reason behind the downward trend in $\langle C_D \rangle$.

Figure 7 shows the variations of $\langle C_D \rangle$, $\langle C_S \rangle$, and $\langle C_{Mz} \rangle$ with yaw angle (β) for the GETS model without base flap. Each of the data plots in this figure has a very high adjusted R-squared value (i.e., Adj. R^2>0.99). That is, proposed regression

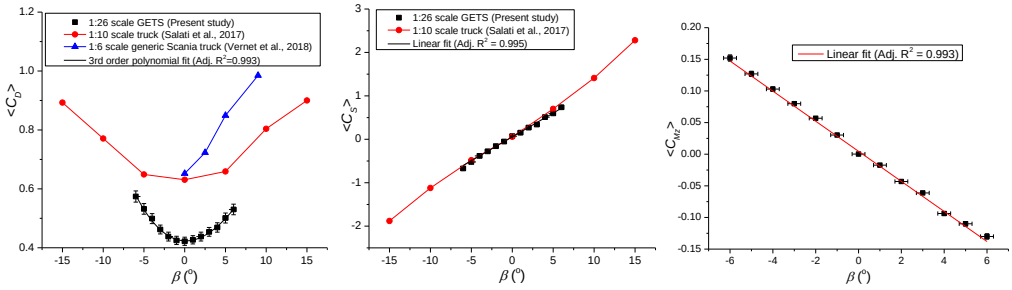

Fig. 7. Variations of time-averaged drag, side, and pitch moment coefficients with yaw angle for the GETS model without base flap (i.e. e00-a00.0-λ00). Re_w=123000±2900. The <C_D> and <C_S> for more realistic tractor-trailer models are shown for comparison.

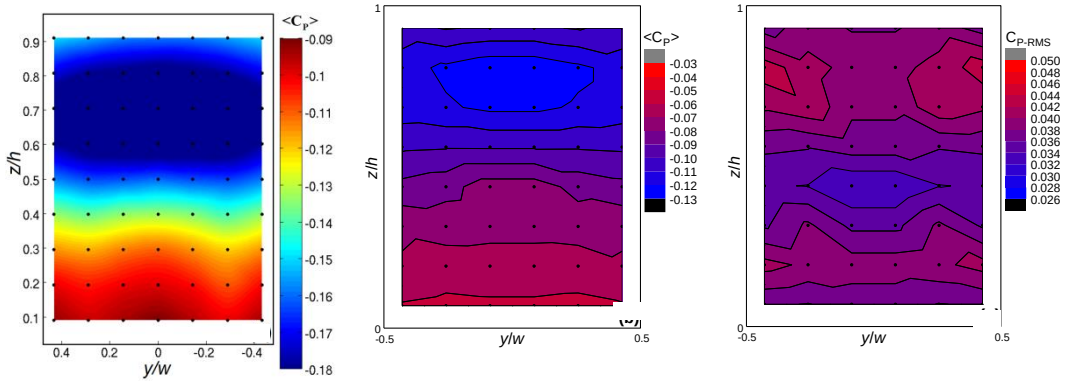

(a) (b) (c)

Fig. 8. (a) Time-averaged pressure coefficient distribution on the base of the GETS model for β=0° and Re_w=710000 (Van Raemdonck 2012). (b) Time-averaged and (c) root-mean-square pressure coefficient distributions on the base of the GETS model without base flap (i.e. e00-a00.0-λ00). β=0° and Re_w=123000±2900.

models perfectly predict all the data points. Force and moment results show strong dependence on the β and good symmetry, but not perfect, between the negative and the positive yaw angles. Similar results were also obtained by several authors whose studies are related to square-back models or vehicles (Gohlke *et al.* 2007; Windsor 2014; McAuliffe 2015; Salati *et al.* 2017). The <C_D> results are, nevertheless, assumed to be the same for both negative and positive yaw angles. This is required to significantly reduce the size of the test matrix. Therefore, force measurements were conducted as a function of positive yaw angles, β=0° to +6°, for the GETS model with a plain or notched base flap.

The <C_D> for the GETS model without a base flap falls to a minimum value of 0.422±0.014 at β=0° (Fig. 7). Irrespective of the yaw angle range studied, the middle and right plots clearly show the existence of a linear trend for side and pitch moment coefficients. In the case of the present simplified model without base flap, the variation of <C_D> and <C_S> with β match closely the more realistic tractor-trailer model (Salati *et al.* 2017; Vernet *et al.* 2018). Figure 8 shows contour plots of time-averaged and root-mean-square coefficients of pressure on the base area of the GETS model without flaps for Re_w=123000±2900. The present <C_P> pattern is qualitatively very similar to that of the Van Raemdonck (2012), despite the large difference in Re_w. It is evident that a low pressure region is concentrated in the central part of the upper half of the base. The lower values of the <C_P> on the upper half of the base reflect that strengths of vortices shed from shear layers from the upper edge of the base are greater than those shed from shear layers from the lower edge. Castelain *et al.* (2018) showed that the base pressure distribution is a function of underbody velocity. As the underbody velocity increases, the lowest pressure region observed on the upper half of the base moves to the lower half. The $C_{P\text{-}RMS}$ level is an important indicator of the unsteady dynamics of the wake. It is evident that regions with higher levels of fluctuations are concentrated in the vicinities of corners of the base. This indicates that strong interactions occur between free shear layers from the top/bottom and lateral edges of the base in the vicinity of the corners. Furthermore, a region with low level of $C_{P\text{-}RMS}$ seen at the mid-height of the base severs the connection between upper and lower regions with high level of $C_{P\text{-}RMS}$. This may be indicative of a bi-stable dynamics of the wake (Grandemange *et al.* 2013; McArthur *et al.* 2016; Perry *et al.* 2016; Rao *et al.* 2018, 2019; Zhang *et al.* 2022a, b). To clarify this, pressure signals in the vicinity of the upper, lower, and side edges of the base were captured (Fig. 9). The trace of bi-stable motion of the wake in the vertical direction is easily detectable by the shift between two stable positions (tap no 9 and 40). On the other hand, there is no

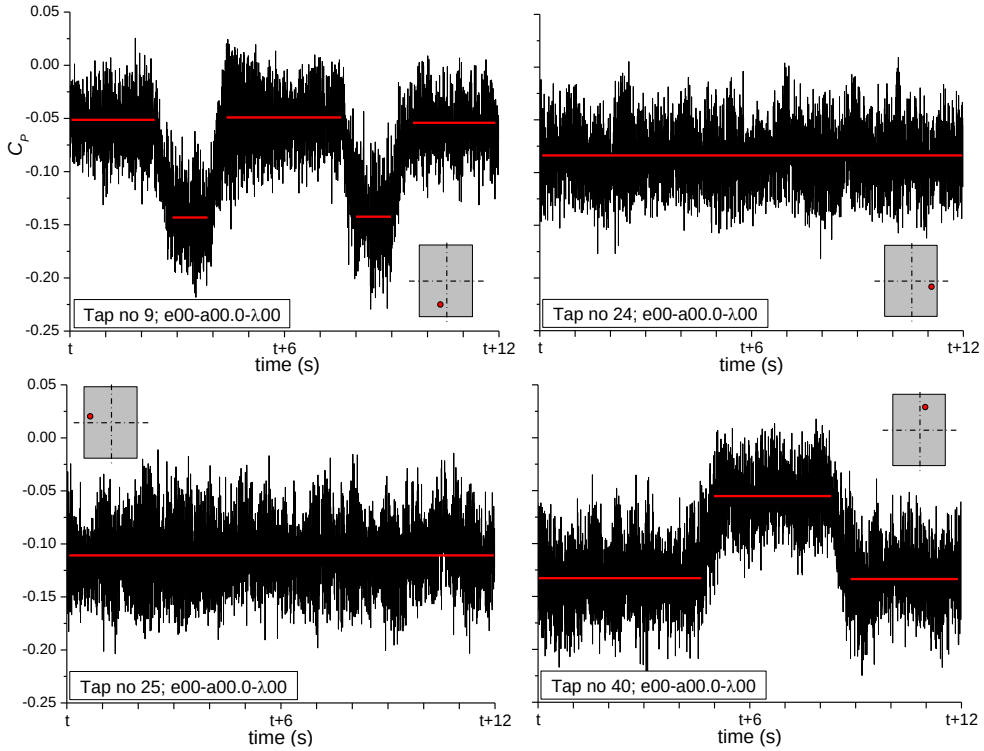

Fig. 9. Time evolutions of the base pressure coefficients at various tap positions for e00-a00.0-λ00. Solid red lines represent local averaging. β=0° and Re_w=123000±2900.

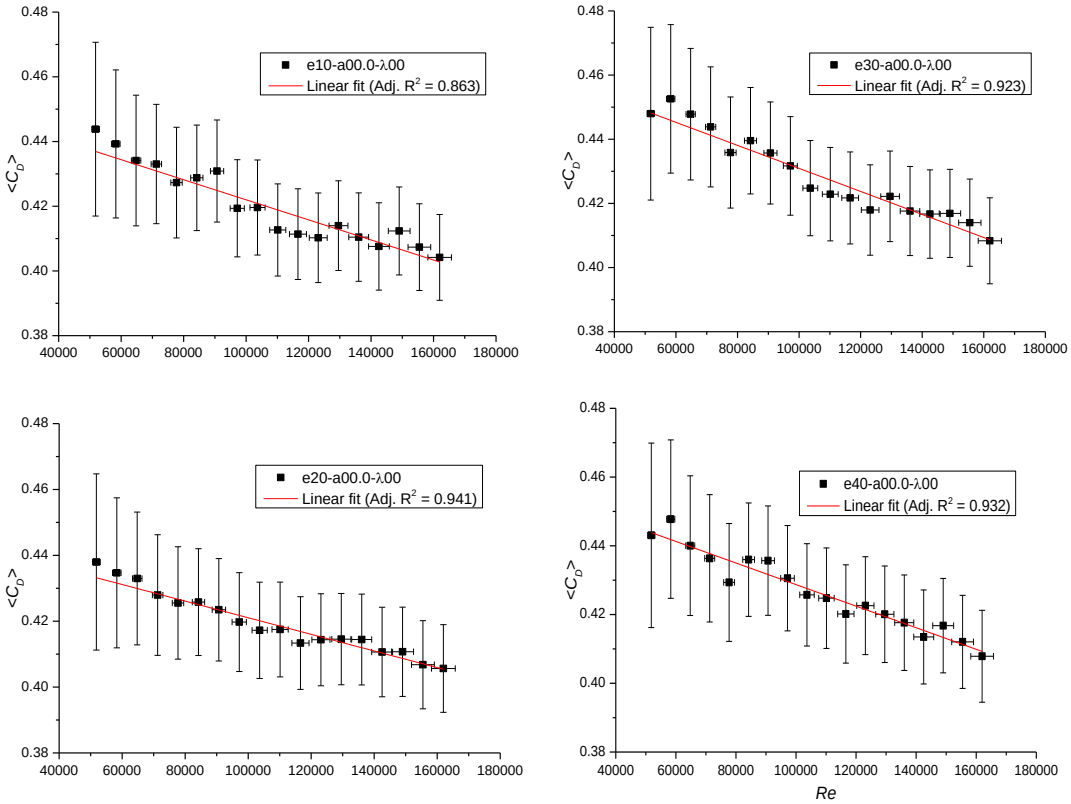

Fig. 10. Measurements of time-averaged drag coefficient versus width-based Reynolds number for a GETS model with various height plain base flaps (i.e. 10, 20, 30, and 40 mm). β=0°. Uncertainties are drawn on graph as error bars.

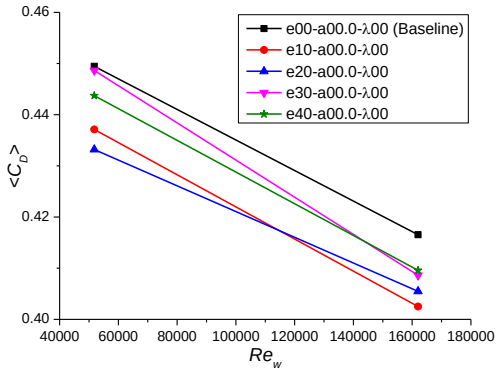

Fig. 11. Comparison of linear fits for GETS model with and without plain base flaps. β=0°.

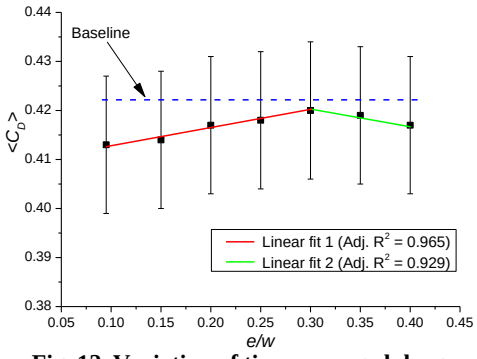

Fig. 12. Variation of time-averaged drag coefficient with dimensionless plain flap length (e/w) for the GETS model. Re_w=123000±2900 and β=0°. Uncertainties are drawn on graph as error bars.

trace of bi-stable motion of the wake in the lateral direction (tap no 24 and 25). The existence of vertical bi-stability and the non-existence of lateral bi-stability in the wake of the baseline GETS were also reported by Schmidt *et al.* (2018).

3.2 Model with Plain Base Flap

Figure 10 displays plots of the time-mean drag coefficient, $\langle C_D \rangle$, versus Re_w for each of the GETS model-plain flap arrangements. In the case of the GETS model fitted with plain base flap, the variation of $\langle C_D \rangle$ with Re_w matches closely the baseline GETS, regardless of the height of plain flap, e (Fig. 6). To make quantitative comparisons of GETS models with and without a plain base flap easier and clearer, linear fits between the $\langle C_D \rangle$ versus Re_w are presented in Fig. 11. A notable feature in Fig. 11 is that regardless of plain flap height GETS model with a plain flap achieves a lower $\langle C_D \rangle$ in comparison with the baseline GETS. A further important feature of Fig. 11 is that the shorter the plain flap height (i.e., e10 and e20) the larger the $\langle C_D \rangle$ reduction.

Figure 12 shows a comparison of the $\langle C_D \rangle$ characteristics for various dimensionless plain flap heights (e/w). The calculated drag coefficients at Re_w=123000±2900 are very close to each other, in spite of the fact that the expanded uncertainties for drag coefficients are providing a level of confidence of approximately 95%. This prevents a definite conclusion about the drag performance of the flaps. However, each of data sets contains 60000 instantaneous data and this number was considered sufficient to calculate the mean drag precisely. Figure 12 is required to explore the optimum plain flap height which minimizes $\langle C_D \rangle$, if exist. The maximum $\langle C_D \rangle$ reduction occurs for e/w=0.1 yielding a drag reduction of 1.9% when compared to the baseline GETS. It is apparent that the $\langle C_D \rangle$ steadily increases until a maximum is reached at e/w=0.3 but then as the dimensionless plain flap height is further increased, the $\langle C_D \rangle$ steadily decreases. The increase in $\langle C_D \rangle$ from e/w=0.1 to 0.3 is partly attributable to the increased skin friction drag with increased plate height. However, the reason for the decrease in $\langle C_D \rangle$ from e/w=0.3 to 0.4 is unclear for now.

Figure 13 shows contour plots of time-averaged coefficients of pressure on the base area of the GETS model with various plain flaps (i.e., e/w=0.2, 0.3, and 0.4, respectively) for Re_w=123000±2900. The $\langle C_P \rangle$ results presented in Fig. 13 show that when the plain flaps are fitted to the base of the GETS model, the region of highest $\langle C_P \rangle$ is shifted upwards, compared to the baseline case. Similar results were observed in the work of Urquhart *et al.* (2018), where $\langle C_P \rangle$ shifted to the center of the base of the SUV model when fitted with three-sided smooth extensions. It is clear that presence of the plain flaps forces the time-averaged bubble to establish a new equilibrium. It is not clear, however, which mechanism is primarily responsible for the reduction in $\langle C_D \rangle$. As e/w increased from 0.1 to 0.3, the region of lowest $\langle C_P \rangle$ is shifted slightly upwards and expanded along the y-axis. On the other hand, the region of highest $\langle C_P \rangle$ is not shifted, but slight local increases in $\langle C_P \rangle$ values are observed. These increases are ascribed to diminished interactions between separated shear layers from the outer sides of the plain flaps and the flow around the base, especially in the vicinity of the upper edge of the base. As e/w increased from 0.3 to 0.4, the region of highest $\langle C_P \rangle$ is remained unchanged. On the other hand, a slight increase in the $\langle C_P \rangle$ in the lower portion of the base is evident. This means that the height of the three-side plain base flap is now long enough to weaken the strength of the vortices from the lower edge of the base. The slight decrease in $\langle C_D \rangle$ as e/w increased from 0.3 to 0.4 is a direct result of this increase in the $\langle C_P \rangle$ in the lower portion of the base.

Figure 14 shows contour plots of root-mean-square coefficients of pressure on the base area of the GETS model with various plain flaps (i.e., e/w=0.2, 0.3, and 0.4, respectively) for Re_w=123000±2900. It is evident that pressure fluctuations on the base are substantially attenuated with the increase in the height of the base plate. That is, wake becomes more stable with the increase in e/w. Figure 15 shows the sensitivity of the vertical bi-stability to e/w. For values up to, and excluding, e/w=0.3, wake showed a certain degree of vertical bi-stability, but for values greater than, and including, e/w=0.3. The

disappearance of the wake bi-stability is found to be the reason for the decrease in $<C_D>$ as e/w increased from 0.3 to 0.4.

3.3 Model with Notched Base Flap

A two-dimensional body has a constant cross-section along the entire span of it. The cross-flow over a two-dimensional body is said to be nominally two-dimensional at a large part of the span when the body is long enough (i.e. span of the two-dimensional body between free ends must be at least ten times greater than its characteristic length). Large-scale vortices formed in the near wake of the two-dimensional bluff bodies are nominally two-dimensional and more organized (Dong *et al.* 2006). On the contrary, the cross-flow over a road vehicle

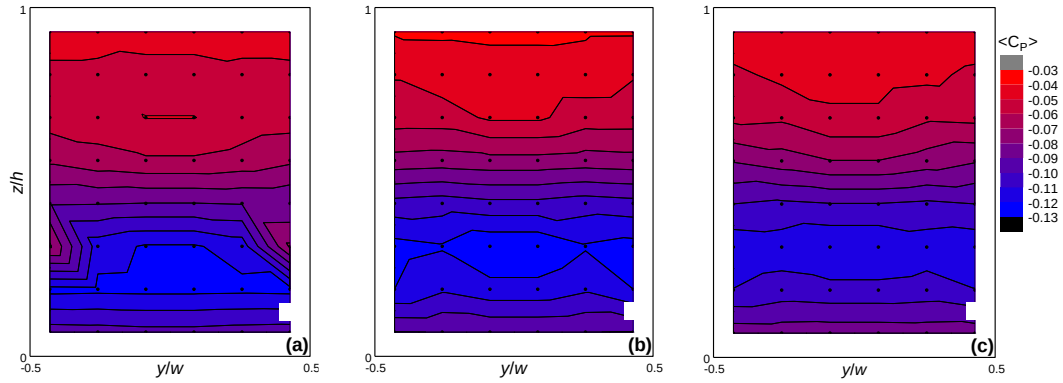

Fig. 13. $<C_P>$ distribution on the base of the GETS model with base flap: (a) e20-a00.0-λ00, (b) e30-a00.0-λ00, and (c) e40-a00.0-λ00. β=0° and Re_w=123000±2900.

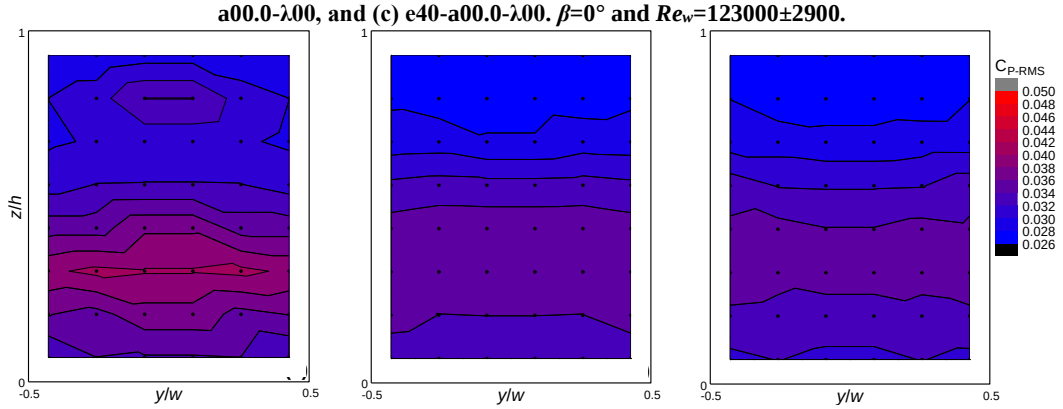

Fig. 14. $C_{P\text{-}RMS}$ distribution on the base of the GETS model with base flap: (a) e20-a00.0-λ00, (b) e30-a00.0-λ00, and (c) e40-a00.0-λ00. β=0° and Re_w=123000±2900.

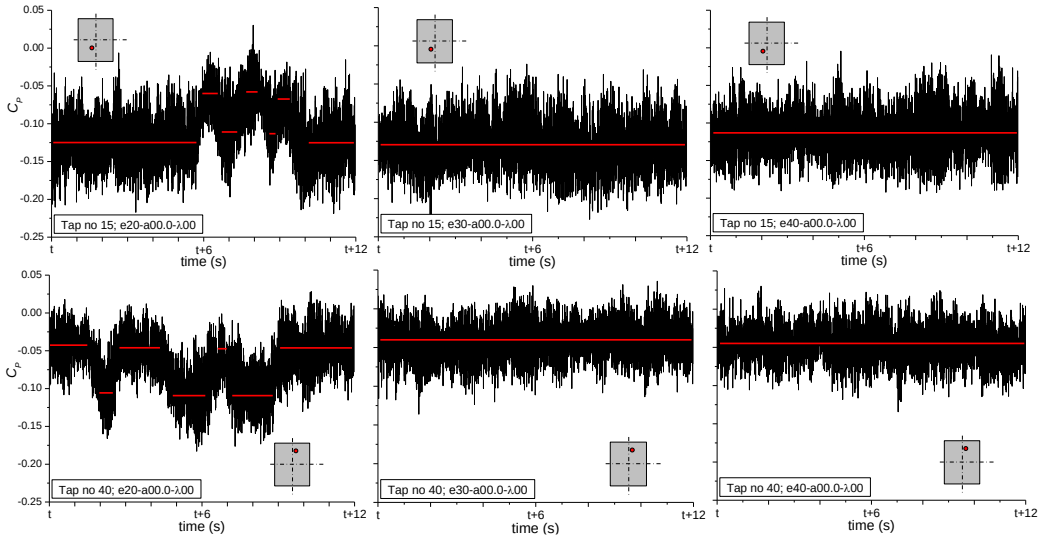

Fig. 15. Time evolutions of the base pressure coefficients at two tap positions (i.e. taps 15 and 40) for e20-a00.0-λ00, e30-a00.0-λ00, and e40-a00.0-λ00, respectively. Solid red lines represent local averaging. β=0° and Re_w=123000±2900.

is three-dimensional and more complex when compared to the two-dimensional body. Therefore, large-scale vortices formed in the near wake of them are three-dimensional and less organized (Perry *et al.* 2016; Dalla Longa *et al.* 2019; Rao *et al.* 2019; Fan *et al.* 2020; Pavia *et al.* 2020).

It has long been known that flow control methods which produce a spanwise variation in the mean straight separation line reduce the $<C_D>$ of a two-dimensional bluff body (Tanner 1972; Tombazis and Bearman 1997). As convincingly explained by Darekar and Sherwin (2001), variation in the mean straight separation line weakens the strength of the spanwise vortex (i.e. large scale vortex formed in the near-wake of the body) by generating transverse and streamwise vortices. This redistribution of vortices leads to an increase in base pressure and a decrease in the time-averaged drag. In this section, the same idea was used for causing the separation lines on the three-dimensional square-back bluff body to deviate from being straight. To this end, a passive flow control method (i.e., three-sided notched flaps) is used to produce a spanwise variation in the fixed straight separation lines at the rear part of the GETS model (i.e., top and lateral edges of the base). The time-averaged drag coefficients, $<C_D>$, are plotted against dimensionless notch amplitude (a/w) and dimensionless notch wavelength (λ/w) for the GETS model in Fig. 16. For comparison, the $<C_D>$ of the baseline model (e00-a00.0-λ00) and of a model with a plain base flap that has the lowest drag (i.e., e10-a00.0-λ00) were considered too. Irrespective of the type of notched plate used, it is evident that the $<C_D>$ of the GETS model with notched base flap is lower than that of the baseline GETS model. For the GETS model with notched base flap the maximum reduction in time-averaged drag coefficient, $\Delta<C_D>=-0.012$, relative to the baseline model, is obtained at a dimensionless notch amplitude of $a/w=0.05$ and a dimensionless notch wavelength $\lambda/w=0.2$ (i.e., e10-a05.0-λ20). The maximum reduction in time-averaged drag coefficient is decreased slightly to $\Delta<C_D>=-0.008$ when a plain base flap (e10-a00.0-λ00) was employed. The results also suggest that as the a/w and λ/w of the notched base flap is reduced, the model vehicle performance improves in terms of drag. The reason for this may be attributed to the formations of more closely spaced small-scale streamwise vortices from the free ends of the notched flaps which possibly lead to the breakdown of the more organized vortical structures within the less three-dimensional separated flow into less organized vortical structures within the more three-dimensional separated flow. A convincing argument could not be put forward since the visualized surface flow patterns on the notched base flaps are not clear. One problem may be the very small size of the notched base plates. Another problem may be the location of the notched base flaps where wall shear stress of the air flow is relatively low. Figures 17 and 18 show contour plots of time-averaged coefficients and root-mean-square coefficients of pressure on the base area of the GETS model with constant amplitude (i.e., $a/w=0.05$) and various wavelength (i.e., $\lambda/w=0.2$ and 0.5) notched flaps, respectively. The $<C_P>$ results presented in Fig. 17 show that when the notched base flap is fitted to the base of the GETS model, the region of lowest $<C_P>$ is shifted downwards, compared to the baseline case. This shift was also observed on the GETS model with a plain base flap (Fig. 13). Another notable feature in this figure is that the lowest $<C_P>$ at the base of the GETS model with e10-a05.0-λ20 is limited to -0.10. However, this value is lower in cases with plain base flaps and e10-a05.0-λ50. This partly explains why $<C_D>$ reaches its lowest level for e10-a05.0-λ20.

The region of highest $C_{P\text{-}RMS}$ is shifted to the centers of lower and upper half parts of the base, compared to the baseline case, when e10-a05.0-λ50 is attached to the base of the model (Fig. 18). Topologically, this pattern is similar to that observed in the base of the model with e20-a00.0-λ00. The same is also true for $<C_P>$ patterns. It can be deduced that a notched base flap with a greater wavelength has the same effect on wake flow as the plain base flap if both have the same height.

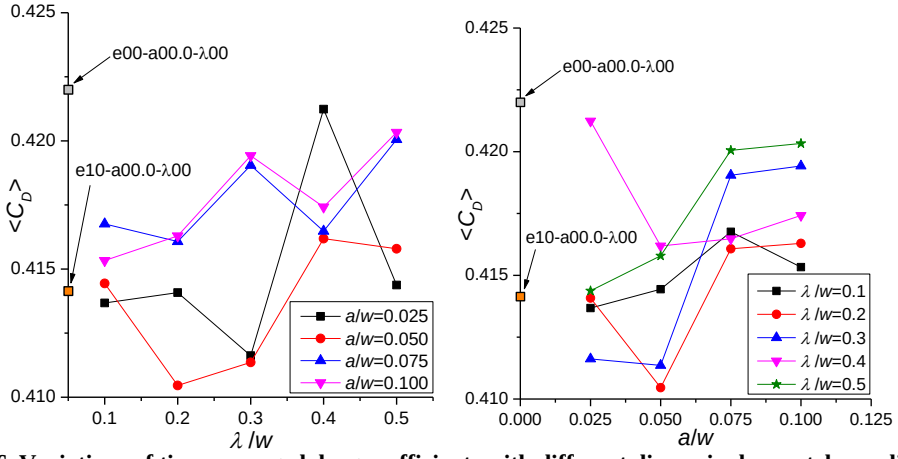

Fig. 16. Variations of time-averaged drag coefficients with different dimensionless notch amplitudes (a/w) and with dimensionless notch wavelengths (λ/w). Re_w=123000±2900 and β=0°. The $<C_D>$s for the model without (baseline) and with a plain base flap (e10-a00.0-λ00) are shown for comparison.

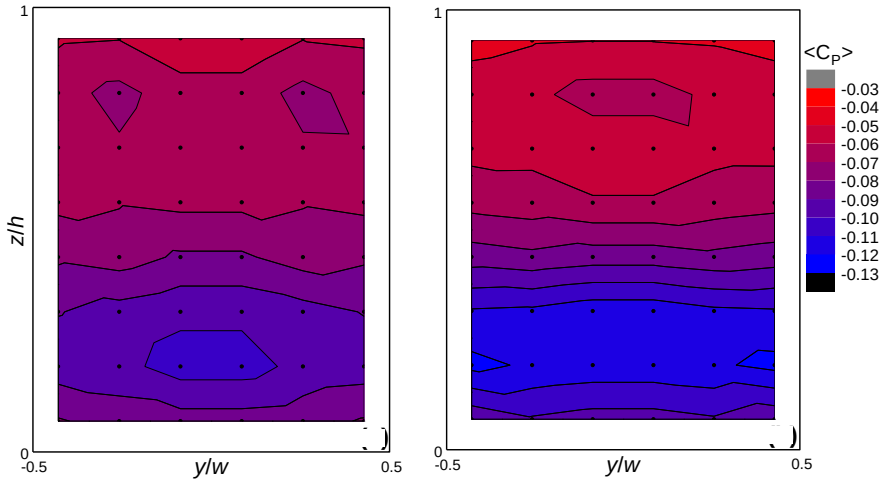

(a) (b)

Fig. 17. <C_P> distributions on the base of the GETS model for two various notched base flaps: (a) e10-a05.0-λ20 and (b) e10-a05.0-λ50. β=0° and Re_w=123000±2900.

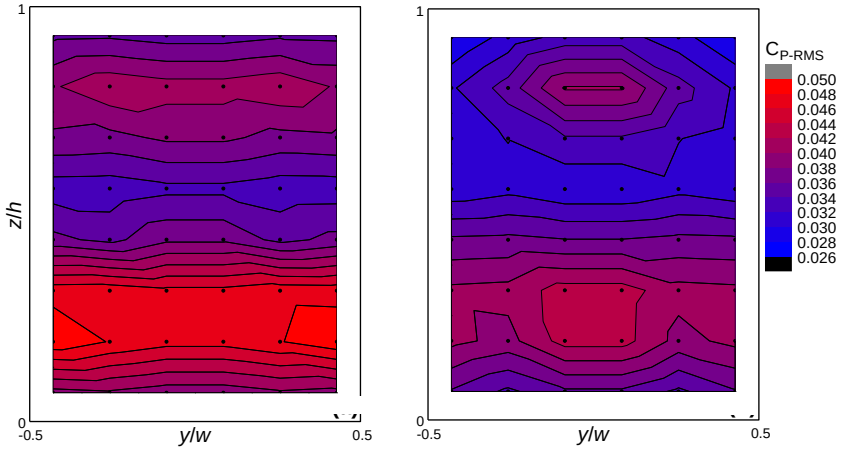

(a) (b)

Fig. 18. $C_{P\text{-}RMS}$ distributions on the base of the GETS model for two various notched base flaps: (a) e10-a05.0-λ20 and (b) e10-a05.0-λ50. β=0° and Re_w=123000±2900.

The level of pressure fluctuations in the base of the GETS model reaches its maximum value when e10-a05.0-λ20 is used. Furthermore, two identifiable concentrations of $C_{P\text{-}RMS}$, one is close to the upper edge, and the other is close to the lower edge of the base, exist along the width of the model with e10-a05.0-λ20. The observation of upper $C_{P\text{-}RMS}$ concentration may be a consequence of increased interactions between small-scale streamwise vortices from the free ends of the neighboring notches. The observation of both upper and lower $C_{P\text{-}RMS}$ concentrations suggests that vertical bi-stability occurs even in the notched base flap case. To justify this proposition, time histories of pressure coefficients at various taps in the base of the model with notched base flaps were plotted (Fig. 19). The existence of the vertical bi-stability (tap no 9 and 40) and the absence of lateral bi-stability (tap no 25) can be seen from Fig. 19.

3.4 Influence of Cross-Wind

It is clear that the most effective plain base flap in reducing drag at zero yaw is e10-a00.0-λ00. It is also clear that the most effective notched base flap in reducing drag at zero yaw is e10-a05.0-λ20. It is known that zero yaw is not entirely representative of the "on-road" environment. Therefore, the aerodynamic effect of implementing these base flaps has been assessed for a range of yaw angles (from β=-6° to +6° in steps of 1°) on the time-averaged drag and side force coefficients (Figs. 20 and 21).

A notable feature in Fig. 20 is that the addition of an e10-a00.0-λ00 or an e10-a05.0-λ20 provided a significant drag reduction at all yaw angles tested. Another notable feature in Fig. 20 is that relative to the no-flap (baseline) case, both flaps significantly reduced the drag by a relatively constant margin for the entire yaw range. The <C_D> curves of the GETS model with e10-a00.0-λ00 and GETS model with e10-a05.0-λ20 were not very similar, except at the higher yaw angles (i.e., $\beta \geq 4$). The addition of the e10-a00.0-λ00 provided a side increase that marginally increased with yaw angle, although the addition of the e10-a05.0-λ20 reduced the side. slightly by a relatively constant margin for the entire yaw range. This suggests that irrespective of

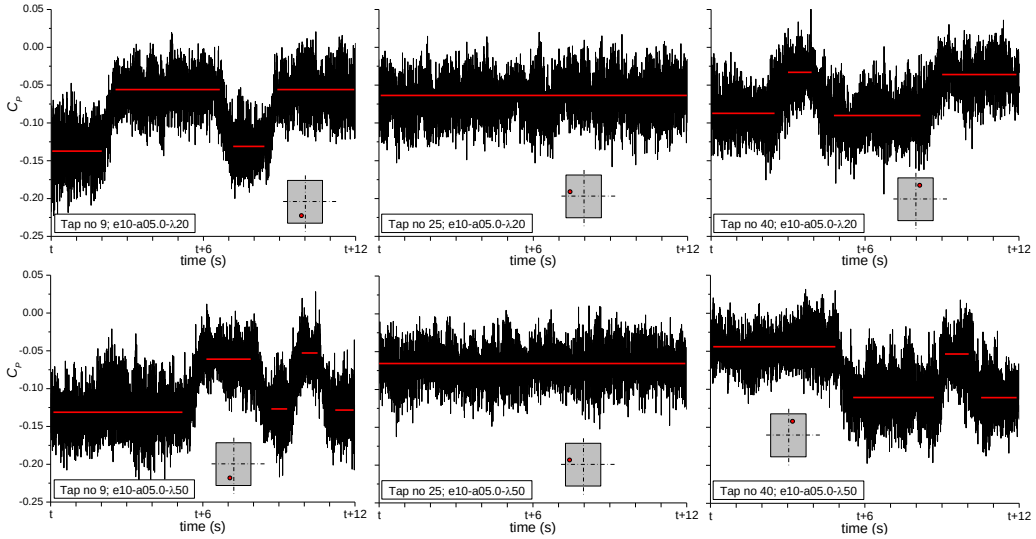

Fig. 19. Time evolutions of the base pressure coefficients at three tap positions (i.e. taps 9, 25, and 40) for e10-a05.0-λ20 and e10-a05.0-λ50, respectively. Solid red lines represent local averaging. β=0° and Re_w=123000±2900.

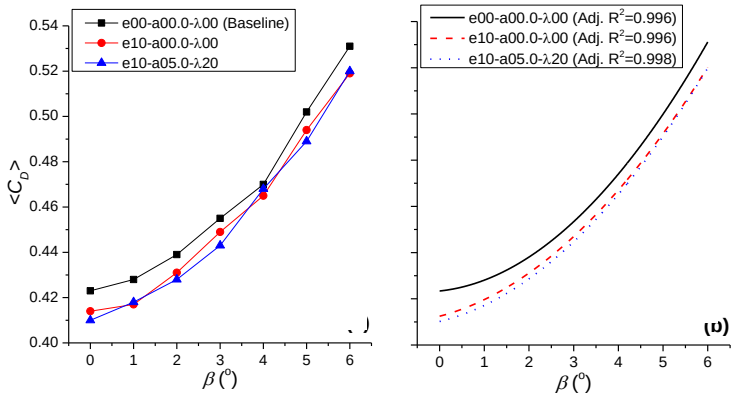

(a) (b)

Fig. 20. (a) A comparison of time-averaged drag coefficients for non-zero yaw angles. Only low drag (i.e. e10-a00.0-λ00 for plain base flap and e10-a05.0-λ20 for notched base flap) and baseline configurations were added. (b) Second-order polynomials were fitted to the data.

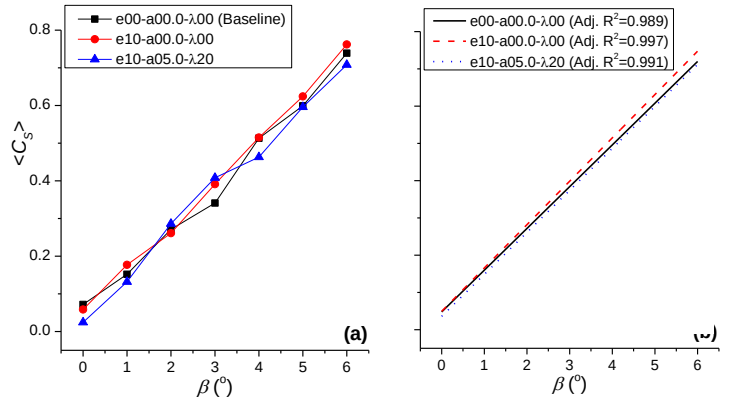

(a) (b)

Fig. 21. (a) A comparison of time-averaged side coefficients for non-zero yaw angles. Only low drag (i.e. e10-a00.0-λ00 for plain base flap and e10-a05.0-λ20 for notched base flap) and baseline configurations were added. (b) First-order polynomials were fitted to the data.

the yaw angle tested, formations of more closely spaced small-scale streamwise vortices from the free ends of the e10-a05.0-λ20 continue to breakdown of the more organized vortical structures into less organized ones in the near wake.

5. CONCLUSION

The most common tractor-trailer combination used in Europe is a semi tractor with two axles and a cargo trailer with three axles. One way of reducing

this vehicles fuel consumption and its carbon dioxide (CO2) emissions is to reduce aerodynamic drag acting on it. One of the main contributors to the aerodynamic drag of this vehicle is base drag, which pulls the vehicle back due to the formation of a low pressure region on the base of the vehicle. This study focuses essentially on this low pressure region. To achieve a base pressure recovery to decrease the time-averaged drag acting on the model, two types of base flap, three-sided plain and notched flaps, were attached to the top, left, and right edges of the base. The current study aims to examine the effects of the dimensionless plain flap height (e/w), dimensionless notch amplitude (a/w), and dimensionless notch wavelength (λ/w) primarily on drag performance of a 1:26 scale Generalized European Transport System (GETS).

To the author's knowledge, the link between the height of the three-sided plain flaps and the time-averaged drag coefficient at zero yaw has not been clearly demonstrated in the literature so far. The bilinear dependence of the $<C_D>$ on the e/w is revealed with a break point at e/w=0.3. More importantly, the lowest $<C_D>$ for the GETS model fitted with a plain base flap is achieved with the smallest e/w tested (i.e., 0.1; e10-a00.0-λ00).

In the case of the GETS model fitted with a plain base flap, the lateral bi-stability was not sensed in the wake of the baseline GETS. On the other hand, the vertical bi-stability resisted up to and, and excluding, e/w=0.3. As the e/w increased from 0.3 to 0.4, bi-stable behavior is no longer evident in the vicinity of the base and the $<C_D>$ started to decrease. That is, the absence of a vertical instability is seen to decrease $<C_D>$.

Base flaps with relatively smaller amplitude and wavelength notches perform best in terms of drag at zero yaw. In this study, the e10-a05.0-λ20 flap shows the best drag performance when compared to the other flaps with/without notches. The addition of this base flap to the GETS model resulted in a 2.8% drag reduction.

The addition of e10-a00.0-λ00 flap to the GETS model significantly reduced the drag by a relatively constant margin for the entire yaw range but slightly increased the side force with increasing yaw angle.

The addition of e10-a05.0-λ20 flap to the GETS model significantly reduced the drag by a relatively constant margin and slightly reduced the side force for the entire yaw range.

In the future, it is planned to move to three-dimensional aerodynamic simulations of a simplified tractor-trailer with base plates to successfully deal with Reynolds number independence problems and to find a link between drag reduction and wake flow characteristics. It is also planned to investigate the effectiveness of base flaps in the presence of spinning wheels and a moving ground plane, which better represent the real-world environment in which road vehicles operate.

ACKNOWLEDGEMENTS

The author would like to thank Dr. Mustafa Sarıoğlu for allowing me to use the wind tunnel facility in the Department of Mechanical Engineering at Karadeniz Technical University. The author also would like to thank Dr. Mehmet Seyhan for all his help for the experimental tests carried out in this paper.

REFERENCES

Beaudoin, J. F. and J. L. Aider (2008). Drag and lift reduction of a 3D bluff body using flaps. *Experiments in Fluids* 44, 491-501.

Browand, F., C. Radovich and M. Boivin (2005). *Fuel Savings by Means of Flaps Attached to the Base of a Trailer: Field Test Results.* SAE Technical Paper.

Capone, A. and G. P. Romano (2019). Investigation on the effect of horizontal and vertical deflectors on the near-wake of a square-back car model. *Journal of Wind Engineering and Industrial Aerodynamics* 185, 57-64.

Castelain, T., M. Michard, M. Szmigiel, D. Chacaton and D. Juve (2018). Identification of flow classes in the wake of a simplified truck model depending on the underbody velocity, *Journal of Wind Engineering and Industrial Aerodynamics* 175, 352-363.

Çengel, Y. A. and J. M. Cimbala (2010). *Fluid Mechanics: Fundamentals and Applications*. 2nd Ed., McGraw-Hill Education, Singapore.

Cerutti, J. J., G. Cafiero and G. Iuso (2021). Aerodynamic drag reduction by means of platooning configurations of light commercial vehicles: A flow field analysis. *International Journal of Heat and Fluid Flow* 90, 108823.

Dalla Longa, L., O. Evstafyeva and A. Morgans (2019). Simulations of the bi-modal wake past three-dimensional blunt bluff bodies. *Journal of Fluid Mechanics* 866, 791-809.

Darekar, R. M. and S. J. Sherwin (2001). Flow past a square-section cylinder with a wavy stagnation face. *Journal of Fluid Mechanics* 426, 263-295.

Dong, S., G. E. Karniadakis, A. Ekmekci and D. Rockwell (2006). A combined direct numerical simulation–particle image velocimetry study of the turbulent near wake. *Journal of Fluid Mechanics* 569, 185-207.

Fan, Y., C. Xia, S. Chu, Z. Yang and O. Cadot (2020). Experimental and numerical analysis of the bi-stable turbulent wake of a rectangular flat-backed bluff body. *Physics of Fluids* 32, 105111.

Garcia de la Cruz, J., R. Brackston and J. Morrison (2017). *Adaptive Base-Flaps Under Variable Cross-Wind. SAE Technical Paper* 2017-01-7000.

Gohlke, M., J. F. Beaudoin, M. Amielh and F. Anselmet (2007). Experimental analysis of flow structures and forces on a 3D-bluff-body in constant cross-wind. *Experiments in Fluids* 43, 579-594.

Grandemange, M., M. Gohlke and O. Cadot (2013). Bi-stability in the turbulent wake past parallelepiped bodies with various aspect ratios and wall effects. *Physics of Fluids*25, 095103.

Haffner, Y., R. Li, M. Meldi and J. Borée (2022). Drag reduction of a square-back bluff body under constant cross-wind conditions using asymmetric shear layer forcing. *International Journal of Heat and Fluid Flow* 96, 109003.

Hanfeng, W., Z. Yu, Z. Chao and H. Xuhui (2016). Aerodynamic drag reduction of an Ahmed body based on deflectors. *Journal of Wind Engineering and Industrial Aerodynamics* 148, 34-44.

Hariram, A., T. Koch, B. Mardberg and J. Kyncl (2019). A study in options to improve aerodynamic profile of heavy-duty vehicles in Europe *Sustainability* 11, 5519.

Hassaan, M., D. Badlani and M. Nazarinia (2018). On the effect of boat-tails on a simplified heavy vehicle geometry under crosswinds. *Journal of Wind Engineering and Industrial Aerodynamics* 183, 172-186.

Hassaan, M., D. Badlani and M. Nazarinia (2020). Numerical study of the effect of aspect ratio on theflow characteristics ofthe Ground Transportation System *Journal of Wind Engineering and Industrial Aerodynamics* 206, 104314.

Kim, D., H. Lee, W. Yi and H. Choi (2016). A bio-inspired device for drag reduction on a three-dimensional model vehicle. *Bioinspiration & Biomimetics* 11, 026004.

Kim, J. J., J. Kim, T. Hann, D. Kim, H. S. Roh and S. J. Lee (2019). Considerable drag reduction and fuel saving of a tractor–trailer using additive aerodynamic devices. *Journal of Wind Engineering and Industrial Aerodynamics* 191, 54-62.

Kowata, S., J. Ha, S. Yoshioka, T. Kato and Y. Kohama (2008). Drag force reduction of a bluff-body with an underbody slant and rear flaps. *SAE International Journal of Commercial Vehicles* 1(1), 230-236.

Landman, D., R. Wood, W. Seay and J. Bledsoe (2010). Understanding practical limits to heavy truck drag reduction. *SAE International Journal of Commercial Vehicles* 2(2), 183-190.

Levin, J. and S. H. Chen (2022). Flow structure investigation of a truck under crosswinds. *Journal of Applied Fluid Mechanics* 15(5), 1513-1523.

Mason, W. T. and P. S. Beebe (1978). The Drag Related Flow Field Characteristics of Trucks and Buses. In G. Sovran, T. Morel, W. T. Mason (Ed.), *Aerodynamic Drag Mechanisms of Bluff Bodies and Road Vehicles*. Springer, Boston, MA.

McArthur, D., D. Burton, M. Thompson and J. Shearidan (2016). On the near wake of a simplified heavy vehicle. *Journal of Fluids and Structures* 66, 293-314.

McArthur, D., D. Burton, M. Thompson and J. Sheridan (2018). An experimental characterisation of the wake of a detailed heavy vehicle in cross-wind. *Journal of Wind Engineering and Industrial Aerodynamics* 175, 364-375.

McAuliffe, B. R. (2015). *Improving the Aerodynamic Efficiency of Heavy Duty Vehicles: Wind Tunnel Test Results of Trailer-Based Drag-Reduction Technologies.* NRC-CNRC Laboratory Technical Report, Report no: LTR-AL-2015-0272.

Patten, J., B. McAuliffe, W. Mayda and B. Tanguay (2012). *Review of Aerodynamic Drag Reduction Devices for Heavy Trucks and Buses.* NRC-CNRC Technical Report, Project no: 54-A3578.

Pavia, G., M. A. Passmore, M. Varney and G. Hodgson (2020). Salient three-dimensional features of the turbulent wake of a simplified square-back vehicle. *Journal of Fluid Mechanics* 888, A33.

Perry, A. K., G. Pavia and M. Passmore (2016). Influence of short rear end tapers on the wake of a simplified square-back vehicle: wake topology and rear drag. *Experiments in Fluids* 57, 169.

Rao, A. N., G. Minelli, J. Zhang, B. Basara and S. Krajnović (2018). Investigation of the near-wake flow topology of a simplified heavy vehicle using PANS simulations. *Journal of Wind Engineering and Industrial Aerodynamics* 183, 243-272.

Rao, A. N., J. Zhang, G. Minelli, B. Basara and S. Krajnović (2019). An les investigation of the near-wake flow topology of a simplified heavy vehicle. *Flow, Turbulence and Combustion* 102, 389-415.

Rejniak, A. A. and A. Gatto (2019). Application of lobed mixers to reduce drag of boat-tailed ground vehicles. *Journal of Applied Fluid Mechanics* 12(6), 1729-1744.

SAE International (1981). SAE Wind Tunnel Test Procedure for Trucks and Buses. Ground Vehicle Standard (J1252_198107).

Salati, L., P. Schito and F. Cheli (2017). Wind tunnel experiment on a heavy truck equipped with front-rear trailer device. *Journal of Wind Engineering and Industrial Aerodynamics* 171, 101-109.

Schmidt, H. J., R. Woszidlo, C. N. Nayeri and C. O.

Paschereit (2015). Drag reduction on a rectangular bluff body with base flaps and fluidic oscillators. *Experiments in Fluids* 56, 151.

Schmidt, H. J., R. Woszidlo, C. N. Nayeri and C.O. Paschereit (2018). The effect of flow control on the wake dynamics of a rectangular bluff body in ground proximity. *Experiments in Fluids* 59, 107.

Seyhan, M. and M. Sarioglu (2021) Investigation of drag reduction performance of half NACA 0009 and 0012 airfoils placed over a trailer on the flow around truck-trailer. *Journal of Mechanical Science and Technology* 35, 2971-2979.

Smith, S., K. Younessi, M. Markstaller, D. Schlesinger, B. Bhatnagar, D. Smith, B. Banceu, R. Schoon, V. K. Sharma, M. Kachmarsky, S. Ghantae, M. Sorrels, C. Deedy, J. Clark and S. Yeakel (2007). *Test, Evaluation, and Demonstration of Practical Devices/Systems to Reduce Aerodynamic Drag of Tractor/Semitrailer Combination Unit Trucks.* Final Report, Contract: DE-FC26-04NT42117.

Storms, B. L., J. C. Ross, J. T. Heineck, S. M. Walker, D. M. Driver and G. G. Zilliac (2001). *An Experimental Study of the Ground Transportation System (GTS) Model in the NASA Ames 7- by 10-Ft Wind Tunnel.*

Sumida, M. and K. Hayakawa (2019). Aerodynamic forces acting on ahmed-type vehicles under fluctuating headwind conditions. *Journal of Applied Fluid Mechanics* 12(5), 1563-1574.

Tanner, M. (1972). A method for reducing the base drag of wings with blunt trailing edge. *Aeronautical Quarterly* 23(1), 15-23.

The Council of The European Union (1996, July). Directive 96/53/EC.

The European Parliament and The Council of The European Union (2015, April). Directive (EU) 2015/719.

The European Parliament and The Council of The European Union (2019, June). Regulation (EU) No 2019/1242.

Tombazis, N. and P. W. Bearman (1997). A study of three-dimensional aspects of vortex shedding from a bluff body with a mild geometric disturbance. *Journal of Fluid Mechanics* 330, 85-112.

Törnell, J., S. Sebben and P. Elofsson (2021). Experimental investigation of a two-truck platoon considering inter-vehicle distance, lateral offset and yaw. *Journal of Wind Engineering and Industrial Aerodynamics*213, 104596.

Urquhart, M., S. Sebben and L. Sterken (2018). Numerical analysis of a vehicle wake with tapered rear extensions under yaw conditions. *Journal of Wind Engineering and Industrial Aerodynamics*179, 308-318.

Urquhart, M., M. Varney, S. Sebben and M. Passmore (2020). Aerodynamic drag improvements on a square-back vehicle at yaw using a tapered cavity and asymmetric flaps. *International Journal of Heat and Fluid Flow* 86, 108737.

Van Raemdonck, G. M. R. (2012). *Design of Low Drag Bluff Road Vehicles*. Ph. D. thesis, Technische Universiteit Delft, the Netherlands.

Van Raemdonck, G. M. R. and M. J. L. Van Tooren (2008). Time-averaged phenomenological investigation of a wake behind a bluff body. In: *6th International Colloquium on Bluff Bodies Aerodynamics and Applications*, Milano, Italy.

Van Straaten, M. (2007). *Computational and Experimental Investigation on Base Drag Reduction of a Generic Transportation System by Guiding Vanes*. M. Sc. thesis, Delft University of Technology, the Netherlands.

Veldhuizen, R., G. M. R. Van Raemdonck and J. P. Van Der Krieke (2019). Fuel economy improvement by means of two European tractor semi-trailer combinations in a platooning formation. *Journal of Wind Engineering and Industrial Aerodynamics* 188, 217-234.

Verband der Automobilindustrie e.V. (VDA) (2010). Commercial vehicles – efficient, flexible, future-proof. Brochure, 17 Sep 2010.

Vernet, J. A., R. Örlü, D. Söderblom, P. Elofsson, and P. H. Alfredsson (2018). Plasma streamwise vortex generators for flow separation control on trucks. *Flow, Turbulence and Combustion* 100, 1101-1109.

Windsor, S. (2014, October). Real world drag coefficient – is it wind averaged drag? In *International Vehicle Aerodynamics Conference 2014*, Loughborough, UK.

Zhang, J., Z. Guo, S. Han, S. Krajnović, J. Sheridan and G. Gao (2022b) An IDDES study of the near-wake flow topology of a simplified heavy vehicle. *Transportation Safety and Environment* 4(2), tdac015.

Zhang, J., F. Wang, S. Han, T. Huang, G. Gao and J. Wang (2022a) An investigation on the switching of asymmetric wake flow and the bi-stable flow states of a simplified heavy vehicle. *Engineering Applications of Computational Fluid Mechanics* 16(1), 2035-2055.